POLYOXOMETALATES

Open Access
RESEARCH ARTICLE

Co_7-cluster metal–organic frameworks for photocatalytic dehalogenation reduction

Sumeng Liu, Saiyu Liu, Yiying Wei, Lanjv Wang, Pengcheng Jiang✉, Haitao Yu✉, and Jianwei Wei✉

Hebei Technology Innovation Center for Energy Conversion Materials and Devices, College of Chemistry and Materials Science, Hebei Normal University, Shijiazhuang 050024, China

Cite This: *Polyoxometalates*, **2026**, *5*, 9140120

Read Online

ABSTRACT: Photocatalytic dehalogenation reduction, which converts a C–X bond into a C–H bond, plays a significant role in synthetic catalysis and pollutant remediation. However, the reduction is significantly affected by photoinduced electron transfer (PET) from organic photoredox catalysts to metal ions or clusters. By introducing photosensitive ligands and cluster-based nodes into metal–organic frameworks (MOFs), we synthesized $Co_7(\mu_3\text{-}O)_3$-cluster MOFs using the easily redox cobalt ions and a tetraphenylbenzene-1,4-diamine-based ligand modified by the central skeleton, effectively regulating the redox potential. The synergistic interactions between the $Co_7(\mu_3\text{-}O)_3$ cluster and the photosensitive ligands enable efficient PET process. This synergy provides a concise strategy for photocatalytic dehalogenation reduction using cobalt-cluster MOFs under mild conditions, which can be extended to aryl halide and halogenated aromatic pollutants.

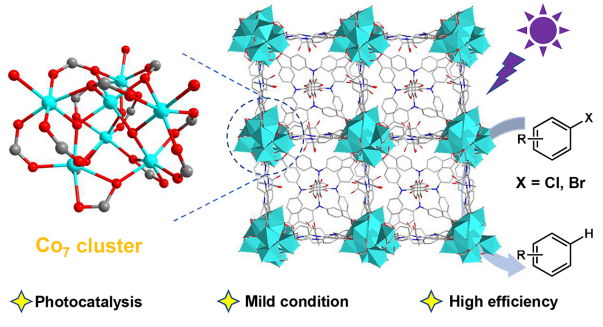

KEYWORDS: metal-organic frameworks, cobalt cluster, photocatalytic dehalogenation, aryl halide

1 Introduction

Chlorinated and brominated aromatics, which are frequently found in industrial wastewater and contaminated soils, constitute a major class of environmental contaminants. These substances are highly toxic, persistent, and bioaccumulative [1–3]. To mitigate the associated environmental risks, significant research efforts have been directed toward developing efficient and practical dehalogenation methods [4–7]. However, this transformation remains one of the most challenging tasks in environmental remediation, which often necessitates harsh reaction conditions [8]. In the past decade, advances in organic photosensitizers and transition metal catalysts have enabled dehalogenative reduction under milder conditions, offering a promising alternative to conventional approaches [9–13]. Despite these advances, the direct integration of photosensitizers with transition metal catalysts still faces three key limitations: achieving high-efficiency photoinduced electron transfer (PET) while minimizing back-electron transfer, preventing photobleaching and self-quenching of excited photosensitizers, and maintaining the stability of transition metal catalysts throughout the catalytic cycle [14–17].

Owing to their tunable structures, high porosity, and well-defined active sites, metal–organic frameworks (MOFs) present an ideal platform to address these challenges [18–21]. A key advantage of MOFs lies in their ability to systematically regulate functionality at the molecular level through framework chemistry [22, 23]. The combination of metal ions or clusters with functionalized organic ligands results in various MOFs with outstanding functions, especially for combining photocatalysis and metal catalysis [24, 25]. Metal clusters with unsaturated coordination sites serve as catalytic centers, and photoactive organic ligands act as photoredox catalysts. This integrated design enables the precise control of PET process between the cluster and the ligands, resulting in high efficiency and minimized back-electron transfer [26–28]. Moreover, immobilizing functional organic dyes as bridging ligands within MOFs effectively suppresses their aggregation and polymerization, thereby preventing self-quenching of the excited state [29, 30].

In MOFs, transition metal ions are usually connected by hydroxide, oxide, water, and carboxylate groups, forming various polyoxometalate (POM) nodes, which enhance the stability of the frameworks [31–37]. POMs are a class of inorganic metal–oxygen cluster compounds characterized by structural tunability, compositional diversity, and efficient electron transfer and storage capabilities. Recently, POM-based MOFs that integrate POM units with metal–organic linkers to form diverse structures have been extensively synthesized, demonstrating broad prospects in catalysis [38–40]. These materials contain POM nodes or metal–oxygen

Received: October 13, 2025; **Revised:** December 31, 2025
Accepted: January 23, 2026

✉Address correspondence to Pengcheng Jiang, pcjiang22@hebtu.edu.cn; Haitao Yu, haitaoyu@hebtu.edu.cn; Jianwei Wei, weijianwei@hebtu.edu.cn

https://doi.org/10.26599/POM.2026.9140120

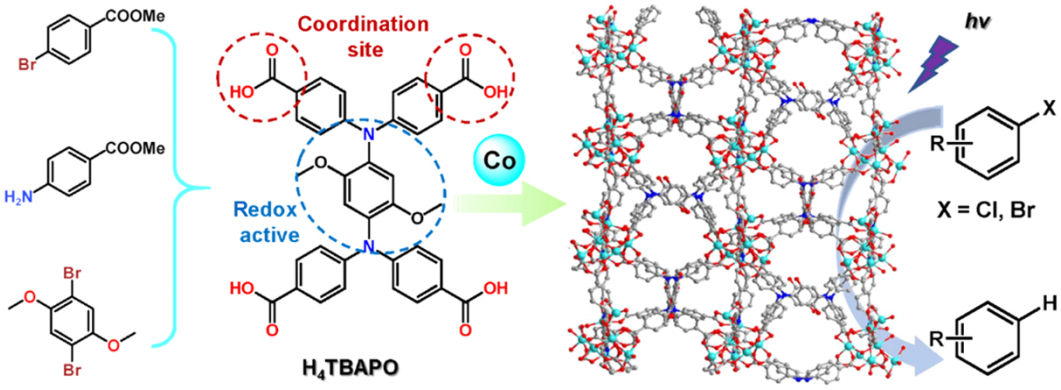

Scheme 1 Schematic diagram of the preparation of cobalt-based cluster MOFs Co-TBAPO for photocatalytic dehalogenation reduction.

clusters structurally similar to POMs, thereby endowing them with multiplemetal catalytic capabilities and multielectron redox activities [41, 42]. Furthermore, cluster-based open metal sites generated after the removal of coordinated solvent molecules often exhibit higher stability than single metal atoms, enhancing the durability of the catalyst during reaction cycles [37]. In addition, the synergistic combination of MOFs and POMs provides a unique heterogeneous platform that integrates molecular-precision catalytic activity, photoredox properties, and the stability of macroscopic materials, thereby extending POM applications to photocatalysis [43, 44].

Inspired by the active center of natural dehalogenase, a cobalt complex with open coordination sites, and its distinctive microenvironment rich in carboxyl groups [45, 46], herein, we synthesized a heptanuclear cobalt cluster-based MOF, denoted as Co-TBAPO, by introducing methoxy groups into a tetraphenylbenzene-1,4-diamine-derived ligand (Scheme 1). Within the framework, the ligands adopt an orderly arrangement without π–π stacking, effectively suppressing the undesired quenching of excited states. The incorporation of electron-donating methoxy groups endows Co-TBAPO with a more negative reduction potential upon photoexcitation. The interconnected cobalt clusters, which are similar to redox-active POM cores, can efficiently accept electrons via PET process. Their polynuclear architecture acts as an electron concentrator, mitigating electron back-transfer. The removal of coordinated water molecules generates open catalytic sites on the clusters, and the robust cluster-based framework ensures structural stability throughout the catalytic cycle. Therefore, the developed heterogeneous cobalt-cluster MOF enables efficient photocatalytic dehalogenation reduction of aryl bromides and chlorides. The system can be extended to halogenated aromatic pollutants, thereby bridging MOF design principles with cluster-based electron-transfer functionality and paving the way for scalable and sustainable POM-inspired photosynthetic strategies.

2 Experimental

2.1 Synthesis of 4,4',4",4"'-((2,5-dimethoxy-1,4-phenylene) bis(azanetriyl))tetra-benzoic acid (H_4TBAPO)

The H_4TBAPO ligand was synthesized via Buchwald–Hartwig coupling of 1,4-dibromo-2,5-dimethoxybenzene and methyl 4-aminobenzoate in xylene, followed by Buchwald–Hartwig coupling with methyl 4-bromobenzoate. The obtained ester was hydrolyzed to form H_4TBAPO as a white solid. Further details of H_4TBAPO synthesis and characterization are provided in the Electronic Supplementary Material (ESM).

2.2 Synthesis of Co-TBAPO

A mixture of $CoCl_2{\cdot}6H_2O$ (0.08 mmol) and H_4TBAPO (0.015 mmol) in N,N-dimethylformamide (DMF, 5.0 mL) with 0.2 mL H_2O and 1.0 mol·L^{-1} HBF_4 (0.1 mL) was added to a 10 mL Parr Teflon-lined vessel. The vessel was capped and heated to 393 K for 60 h. The resulting mixture was cooled to room temperature, and violet block crystals were obtained (yield: 56%. CCDC: 2494127. Anal. Calcd. for $C_{36}H_{26}Co_{2.33}N_2O_{12}$: C, 52.99; H, 3.21; Co, 16.83; N, 3.43. Found: C, 52.19; H, 3.54; Co, 15.95; N, 3.83).

2.3 Photoinduced dehalogenation reduction

Co-TBAPO (1.0 μmol), aryl halide (0.15 mmol), morpholine (0.6 mmol), and HCOOH (0.6 mmol) in *N,N*-dimethylacetamide (DMAc, 5 mL) were added to a 20 mL flame-dried Schlenk quartz flask. The flask was degassed by bubbling argon for 15 min at room temperature under atmospheric pressure. After that, the samples were irradiated using a 50 W LED lamp at 395 nm, and the reaction temperature was maintained at 298 K by using a water filter to absorb the heat. The yields of the crude products were determined by gas chromatography (GC) analysis using 1,3,5-trimethoxybenzene as the internal standard.

3 Results and discussion

3.1 Characterization of Co-TBAPO

Single crystal X-ray diffraction structural analysis revealed that Co-TBAPO adopts a three-dimensional (3D) structure and crystallizesin the *R*32 trigonal space group. All cobalt ions in the framework exhibit octahedral coordination geometry (Fig. 1(a) and Fig. S1 in the ESM). Co01 is six-coordinated with three μ_3-O^{2-} and three carboxylate oxygen atoms of three $TBAPO^{4-}$ ligands. Co02 is coordinated with five carboxylate oxygen atoms and one O^{2-}. Similarly, Co03 is six-coordinated with one O^{2-}, one water oxygen atom, and four carboxylate oxygen atoms from four $TBAPO^{4-}$ ligands. Each O^{2-} bridges three Co atoms to form a $Co_3(\mu_3\text{-}O)$ tetrahedron, and three such tetrahedra are fused via vertex sharing of Co01 to form a C_3 symmetric twisted triangular prism $Co_7(\mu_3\text{-}O)_3(OOC\text{-})_{12}$ cluster, with the remaining coordination sites capped by nine carboxylate groups and three water molecules (Fig. 1(b)). For balanced charges, the seven Co ions must contain 18 positive charges, indicating four Co(III) ions in the $Co_7(\mu_3\text{-}O)_3$ cluster. The

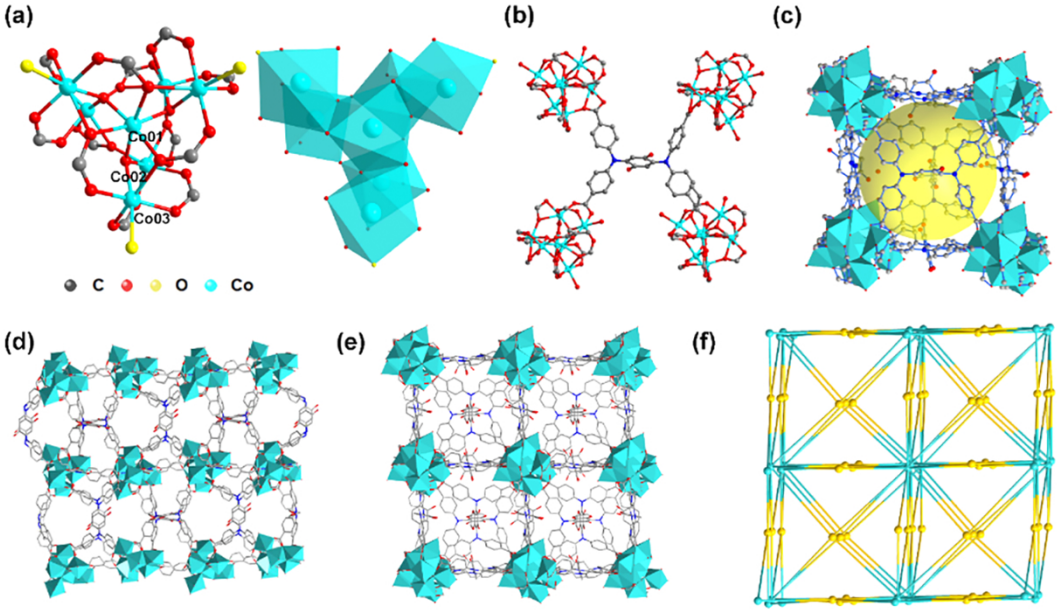

Figure 1 (a) Trigonal $Co_7(\mu_3\text{-}O)_3(OOC\text{-})_{12}$ cluster. (b) Bridging coordination mode of ligands. (c) The cubic cavity of Co-TBAPO. Three-dimensional framework of Co-TBAPO showing (d) the channels and (e) the repeat unit. (f) The dfs topology of Co-TBAPO. Color scheme: C, gray; N, blue; Co, cyan; and O, red and yellow.

six $TBAPO^{4-}$ ligands connected to eight $Co_7(\mu_3\text{-}O)_3$ clusters form a cubic cage with an internal cavity of 14 Å × 14 Å × 14 Å (Fig. 1(c)), providing a favorable microenvironment for photocatalytic reactions. Each $Co_7(\mu_3\text{-}O)_3$ cluster is located at the apex of the cubic cavity, and the coordinated water molecules on it extend to the interior of the cavity. By removing the water molecules, the $Co_7(\mu_3\text{-}O)_3$ cluster forms an empty Co active center similar to dehalogenase, and the structure of the cluster ensures the stability of the skeleton during catalysis [47]. The nine coordinated carboxyl groups on the $Co_7(\mu_3\text{-}O)_3$ cluster ensure structural stability and provide an enzyme-like microenvironment. In addition, its multiple open-type channels facilitate the diffusion of reactants and products (Fig. 1(d)) [48]. As a repeat unit, the cage is further extended into a microporous 3D framework with a dfs topology (Figs. 1(e) and 1(f)) [49]. Upon the removal of guest molecules, the Co-TBAPO structure exhibits a porosity of ~ 49.8% and a void volume of about 12,830 $Å^3$ per unit cell (calculated using PLATON [50]). The Brunauer–Emmett–Teller (BET) surface area and average pore width of the framework are 10.682 $m^2 \cdot g^{-1}$ and 1.410 nm, respectively (Figs. S2 and S3 in the ESM). The pore volume of the BET test was consistent with that recorded by single-crystal X-ray diffraction analysis, indicating that the pore channels of Co-TBAPO are large enough for the smooth diffusion of substrates into MOFs.

Thermogravimetric analysis (TGA) revealed that Co-TBAPO did not decompose below 430 °C (Fig. S5 in the ESM), indicating that Co-TBAPO maintained a stable structure at room temperature. In addition, it was capable to activate Co-TBAPO by removing coordinated water molecules through tolerating heat. The impressive solvent weight loss of 6.2% for Co-TBAPO in the temperature range of room temperature to 430 °C can be attributed to the removal of three coordinated water molecules of the $Co_7(\mu_3\text{-}O)_3$ cluster and one free solvent DMF molecule in the cavity [10]. We infer that Co-TBAPO can form empty coordination cobalt nodes by removing some of the coordinated water molecules, which enables the activation of the substrate, thereby promoting the reaction through interactions with unsaturated cobalt clusters [30]. Therefore, the Co-TBAPO crystal was treated under a vacuum at 70 °C for 2 h to obtain activated Co-TBAPO. The powder X-ray diffraction (PXRD) patterns of Co-TBAPO revealed the phase purity of the bulk sample after synthesis (Fig. 2(a) and Fig. S4 in the ESM). The PXRD spectra of Co-TBAPO before and after treatment were similar, indicating that the structure was retained after activation [51]. TGA of the activated Co-TBAPO revealed thermal stability similar to that of the unactivated framework and a gradual solvent weight loss of 5.2 wt.% as the temperature increased from room temperature to 430 °C (Fig. S5 in the ESM). The weight loss can be attributed to the removal of various solvent molecules with hydrogen-bonding interactions in the cavity, further indicating the elimination of coordinated water molecules during activation [30]. The empty coordination sites of the activated Co-TBAPO enable the activation of substrates for synergistic catalysis [52]. Fourier transform infrared (FT-IR) spectroscopy also revealed that Co-TBAPO exhibited no significant changes after activation, except for the loss of the broad peak of the O–H bands (approximately 3670–3100 cm^{-1}) for water molecules (Fig. 2(b) and Fig. S7 in the ESM). These results are consistent with the *in situ* test results (Fig. 2(c) and Fig. S8 in the ESM). The intensity of the characteristic peak at ~ 3450 cm^{-1} (O–H stretching vibration) decreased significantly, indicating the removal of the coordinating water molecules in Co-TBAPO. After activation, XRD revealed that the activated Co-TBAPO maintained the original framework, ensuring sufficient structural stability for synergistic photoredox catalysis.

The morphological characteristics of Co-TBAPO after grinding were obtained by scanning electron microscopy (SEM). The SEM images show dark-purple block crystals with a size of 300–500 nm (Fig. 2(d)). The mapping spectrum revealed that O, N, C, and Co were distributed within the structure (Fig. 2(d) and Fig. S9 in the ESM), consistent with the energy-dispersive X-ray spectroscopy (EDS) results (Fig. S10 in the ESM). The solid-state ultraviolet–visible (UV–Vis) spectra of Co-TBAPO exhibited strong absorption bands spanning a broad range of 200–450 nm (Fig. 3(a)), which can be attributed to the H_4TBAPO ligands. The new bands over 600 nm are typical d–d transition peaks of $Co_7(\mu_3\text{-}O)_3$ clusters [53]. These broad absorption bands of Co-TBAPO

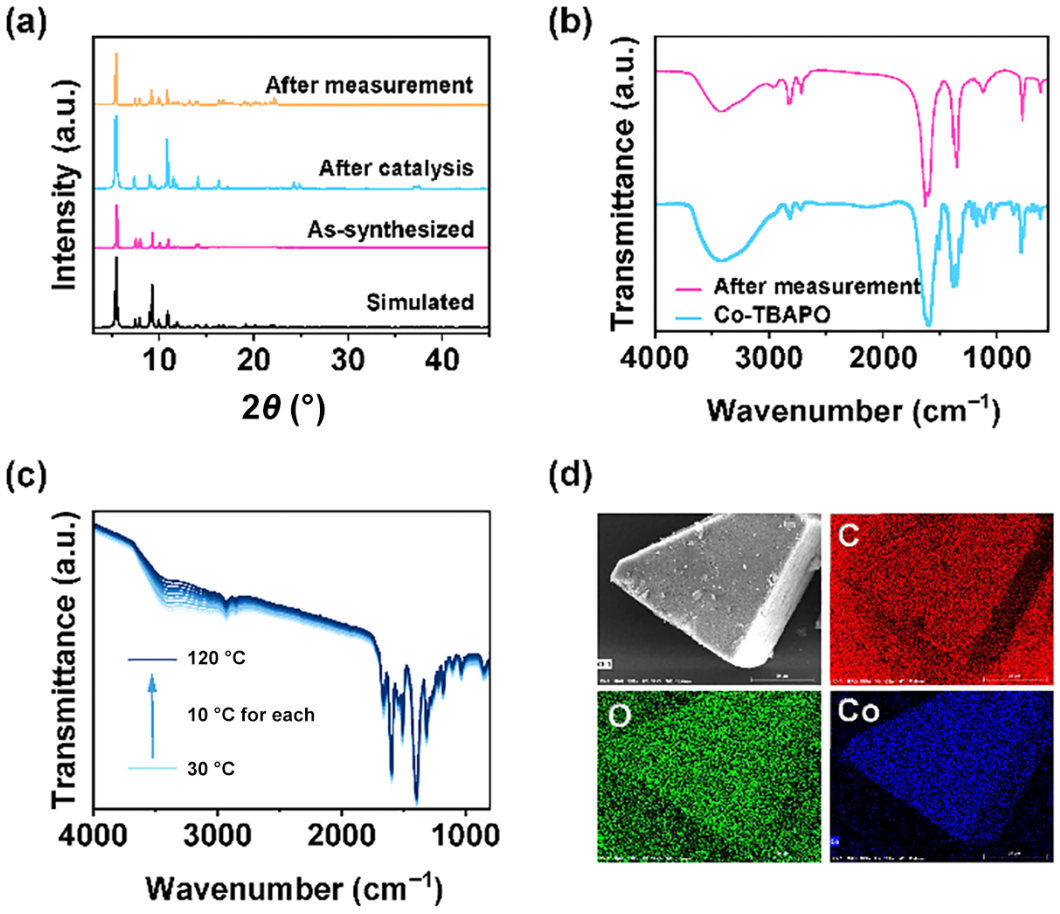

Figure 2 (a) PXRD patterns of the single-crystal simulated Co-TBAPO (black), the fresh as-synthesized Co-TBAPO (pink), Co-TBAPO after measurement for activation (orange), and the recycled Co-TBAPO after catalysis (cyan). (b) FT-IR spectra of Co-TBAPO as-synthesized (cyan) and after measurement (pink). (c) *In situ* IR spectra of Co-TBAPO with heating from 30 to 120 °C. (d) SEM image and annular-dark-field EDS element mapping of Co-TBAPO elemental, with Co (blue), O (green) and C (red).

indicate promising potential for light harvesting under UV/visible irradiation. The spectra showed significant absorption up to 395 nm, indicating that the cobalt-based MOFs are photoactive under 395-nm irradiation. Based on the Kubelka–Munk formula, a bandgap of 2.71 eV was estimated from the Tauc plot of the UV–vis spectra of Co-TBAPO, indicating that the MOF can be excited under 395-nm illumination (Fig. 3(a)). Mott–Schottky measurements of Co-TBAPO were conducted at frequencies of 1000, 2000, and 3000 Hz, and the positive slope of the C^{-2} values (vs. applied potentials) indicates an n-type semiconductor (Fig. 3(b)). The flat band potential of the MOFs derived from the frequency intersection point was −1.84 V vs. Ag/AgCl, consistent with the cyclic voltammetry (CV) test results (Fig. S18 in the ESM). The CV tests on H_4TBAPO showed a reduction potential of −2.10 V vs. Ag/AgCl (Fig. S17 in the ESM). Considering that the bottom of the conduction band (i.e., the lowest unoccupied molecular orbital, LUMO) in n-type semiconductors is approximately 0.2 V above the flat band [54], the LUMO of Co-TBAPO is located at approximately −1.64 V vs. NHE. The corresponding highest occupied molecular orbital (HOMO) was then calculated to be 1.07 V vs. NHE (Fig. 3(d)), which is consistent with the valence band test via X-ray photoelectron spectroscopy (XPS) (Fig. S15 in the ESM). The luminescence emission spectra of H_4TBAPO were also measured at room temperature with an excitation wavelength of 395 nm, and green luminescence was observed at 500 nm (Fig. S12 in the ESM). The excited-state energy $E^{0\text{-}0}$ of H_4TBAPO determined from the cross point of the UV–vis absorption and fluorescence spectra at 417 nm was 2.97 eV. The LUMO of H_4TBAPO was located at approximately −1.90 V vs. NHE (Fig. S12 in the ESM), and the HOMO was 1.07 V vs. NHE (Fig. 3(d)). Such an energy-band structure makes Co-TBAPO theoretically suitable for facilitating photoinduced dehalogenation reactions [55]. Furthermore, the addition of an electron agent into the DMAc suspension containing H_4TBAPO quenched approximately 20% of the emission intensity (Fig. 3(e)). The fluorescence lifetime of the ligand decreased from 2.68 to 1.29 ns after the addition of formic acid (Fig. 3(f)). The lifetime of Co-TBAPO was shorter than that of the ligands upon the addition of formic acid, with the fluorescence intensity becoming almost unmeasurable, indicating that the photosensitive ligand can absorb light and give out electrons to the $Co_7(\mu_3\text{-}O)_3$ clusters through photoinduced metal to ligand charge transfer (MLCT) process, forming a highly redox-active cluster catalyst for dehalogenation reactions. The oxidized ligands are regenerated by obtaining electrons from the electron agent [56].

The transient photocurrent responses of Co-TBAPO showed a reproducible photocurrent upon the on/off cycles of the 395-nm LED irradiation (Fig. 3(g)), suggesting that Co-TBAPO exhibits high electron–hole separation efficiency [57]. Furthermore, electrochemical impedance spectroscopy (EIS) revealed that Co-TBAPO exhibits lower electron transport resistance (R_{ct},

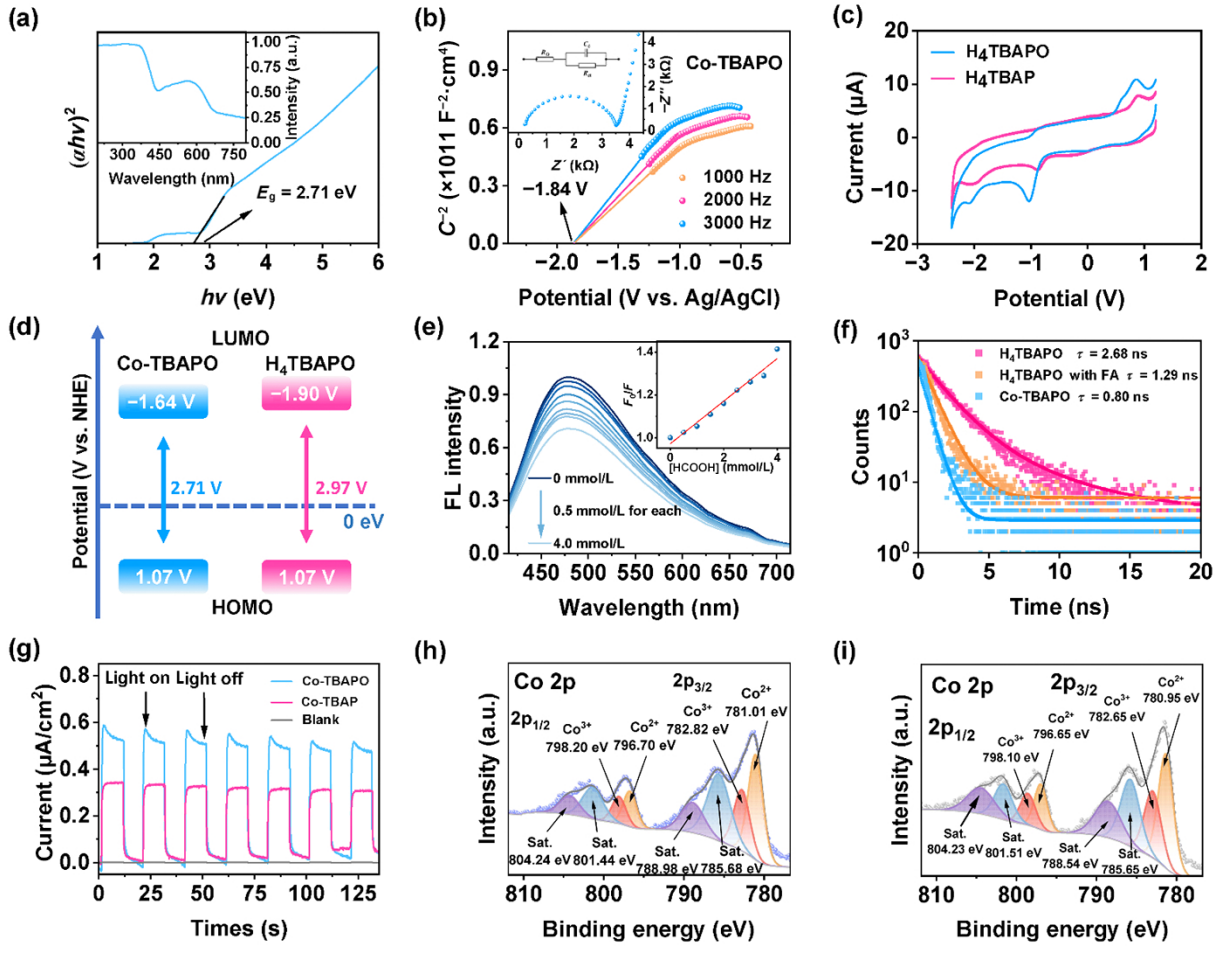

Figure 3 (a) UV–vis spectrum and (inset) the Tauc plot of Co-TBAPO. (b) Mott–Schottky plots and (inset) EIS Nyquist plot of Co-TBAPO at 1000, 2000 and 3000 Hz. (c) Cyclic voltammogram of H_4TBAPO (0.1 mmol/L) and H_4TBAP (0.1 mmol/L) in DMAc. (d) The diagrams of HOMO and LUMO levels of Co-TBAPO and H_4TBAPO. (e) Fluorescence quenching spectra of H_4TBAPO in DMAc suspension upon the addition of HCOOH and (inset) the corresponding simulated Stern–Volmer curve. (f) The PL decay curves of H_4TBAPO, H_4TBAPO with HCOOH and Co-TBAPO. (g) Photocurrent signals of Co-TBAPO (blue) and Co-TBAP (pink). XPS spectra of of Co 2p of Co-TBAPO (h) before and (i) after illumination.

approximately 3.5 kΩ) than Co-MOFs (Fig. 3(b)), indicating that rapid electron transfer in Co-TBAPO, which promotes efficient photocatalytic reactions [58]. The XPS spectra of Co-TBAPO confirmed the +2 and +3 two-type states of the Co element in MOFs (Fig. 3(h)), with Co(II) $2p_{3/2}$, Co(III) $2p_{3/2}$, Co(II) $2p_{1/2}$, and Co(III) $2p_{1/2}$ peaks at 781.01, 782.82, 796.70, and 798.20 eV, respectively, and distinct satellite peaks (785.68, 788.98, 801.44, and 804.24 eV, respectively) [59]. Fine peak fitting showed that the relative atomic percentage of Co(II) species was 45%, which is consistent with the calculated proportion of Co(II) in the crystal. The O 1s peaks centered at 531.08, 531.86, and 533.17 eV are assigned to Co–O bonds, C–O bonds of central benzene, and –COOH, indicating that Co ions and oxygen atoms are coordinated in the MOFs (Fig. S13 in the ESM). Because of the forced torsion between the metal nodes and the ligands, Co ions in Co-TBAPO polymerize to form electron-deficient $Co_7(\mu_3\text{-}O)_3$ clusters, resulting in a lower charge density surrounding the catalytically active cluster. Co-TBAPO emitted negligible fluorescence, indicating that cobalt clusters facilitate the smooth transfer of the excited electrons on the ligand to the $Co_7(\mu_3\text{-}O)_3$ clusters. Clusters with both Co(II) and Co(III) can efficiently accumulate electrons and promote reduction. After 395-nm illumination, the Co-TBAPO XPS data showed that the Co $2p_{3/2}$ and Co $2p_{1/2}$ peaks red-shifted by 0.1–0.2 eV (Fig. 3(i) and Fig. S14 in the ESM). Fine peak fitting revealed that the relative atomic percentage of Co(II) increased significantly (from 45% to 56%), indicating that electrons were transferred from photosensitive ligands to the center of the Co_7 cluster, resulting in the partial reduction of Co(III) to Co(II). Therefore, ligand-regulated cobalt-cluster MOFs for synergistic photocatalysis can be achieved.

3.2 Photocatalytic dehalogenation of aryl halides

We conducted experiments to investigate the photocatalytic performance of the proposed Co-cluster MOFs using C–X dehalogenation reactions as the benchmark. Under standard experimental conditions, the reactions occurred at room temperature in a quartz flask containing ethyl 4-chlorobenzoate **1** (0.15 mmol), morpholine (0.6 mmol), and HCOOH (0.6 mmol) in a DMAc (5.0 mL) solution. The loading of 1.0 μmol of Co-TBAPO in argon under irradiation with a 395-nm LED for 5 h resulted in the formation of ethyl benzoate **1a** at a yield of approximately 93% (Table 1, entry 1). Replacing **1** with ethyl 4-bromobenzoate under similar reaction conditions, **1a** was also obtained at a good yield (98%) (Table 2). Without Co-TBAPO or light (control experiments), no reaction was recorded (Table 1, entries 2 and 3). With light, the activity of the catalytic systems for the formation of

Table 1 Control experiments of photocatalytic dehalogenation with Co-TBAPO[a]

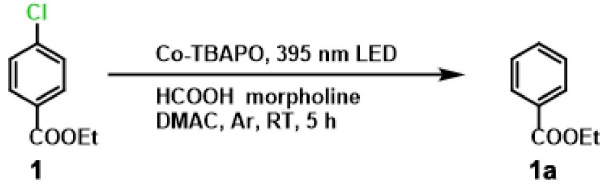

Entry	Conditions	Yield (%)
1	No change with standard conditions	93
2	No catalyst	N.R.
3	No light	N.R.
4	50 °C instead of rt	93
5	air instead of Ar	N.R.
6	420 nm LED	trace
7	DABCO instead HCOOH	58
8	0.5 equiv HCOOH morpholine	47
9	$CoCl_2{\cdot}6H_2O$	trace
10	un-activated Co-TBAPO	62
11	H_4TBAPO/$CoCl_2{\cdot}6H_2O$ as catalyst	46

[a]Reaction conditions: ethyl 4-chlorobenzoate (0.15 mmol), morpholine (0.6 mmol), HCOOH (0.6 mmol), and Co-TBAPO (1.0 μmol) in DMAc (5.0 mL) under irradiation with a 395 nm LED in argon atmosphere within 5 h.

1a at 50 °C was not improved (Table 1, entry 4), indicating that photocatalytic dehalogenation is not a thermodynamically driven reaction [12]. The catalytic system exhibited poor performance in the air (Table 1, entry 5), and in the presence of 420 nm LED light, it exhibited no activity for the formation of **1a** (Table 1, entry 6). Replacing HCOOH with 1,4-diazabicyclo[2.2.2]octane or reducing the amount of electron agent reduced the reaction efficiency (Table 1, entries 7 and 8). By changing the loading of the catalyst Co-TBAPO, the yields gradually decreased following the catalyst reduction (Fig. S16 in the ESM). When $CoCl_2{\cdot}6H_2O$ was used as a catalyst (Table 1, entry 9), no activity for the formation of **1a** was recorded, indicating that free cobalt ions are not the main active species. Using the unactivated MOFs as the catalyst, the yield of **1a** decreased from 93% to 62% (Table 1, entry 10).

Furthermore, when H_4TBAPO was used as the photocatalyst, **1a** yield further decreased to 41%, with over 50% of the reactants remaining under the same conditions (Fig. 4(a)). Using a physical mixture of H_4TBAPO and $CoCl_2{\cdot}6H_2O$ afforded **1a** at only a 46% yield (Table 1, entry 11). These results indicate that the cobalt clusters in the proposed MOF improve the reaction activity of the catalyst. To verify this process, we compared the proposed framework with Co-TBAP [51], which contains $Co_8(\mu_4\text{-}O)_3$ clusters, a similar diphenylamine ligand, and three more concealed coordination water molecules than Co-TBAPO. The reduction potential of H_4TBAP is positive compared with that of H_4TBAPO (Fig. 3(c)). Because photoinduced excitons have good activity only after effective charge separation, Co-TBAPO exhibited better photocurrent response characteristics than Co-TBAP, indicating

Table 2 Photocatalytic dehalogenation of aryl halides with Co-TBAPO photocatalytic system[a]

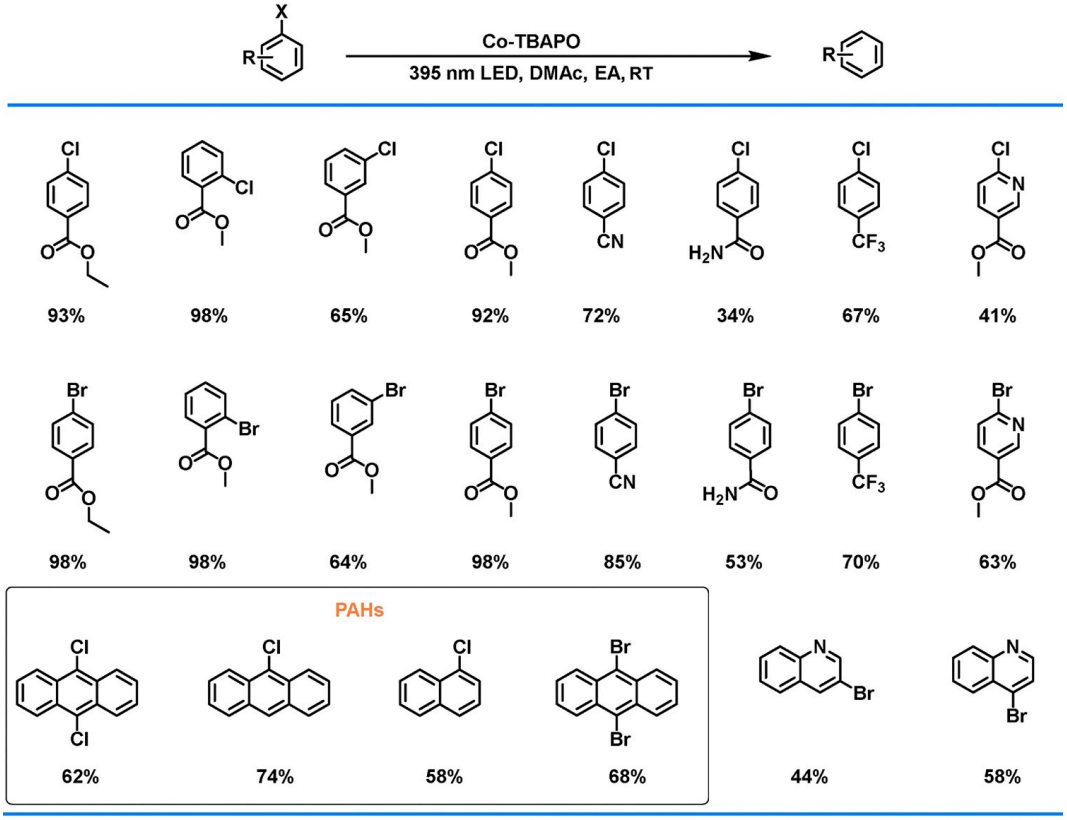

[a]Reaction conditions: substates (0.15 mmol), morpholine (0.6 mmol), HCOOH (0.6 mmol), and Co-TBAPO (1.0 μmol) in DMAc (5.0 mL) under irradiation with a 395 nm LED in argon atmosphere within 5 h.

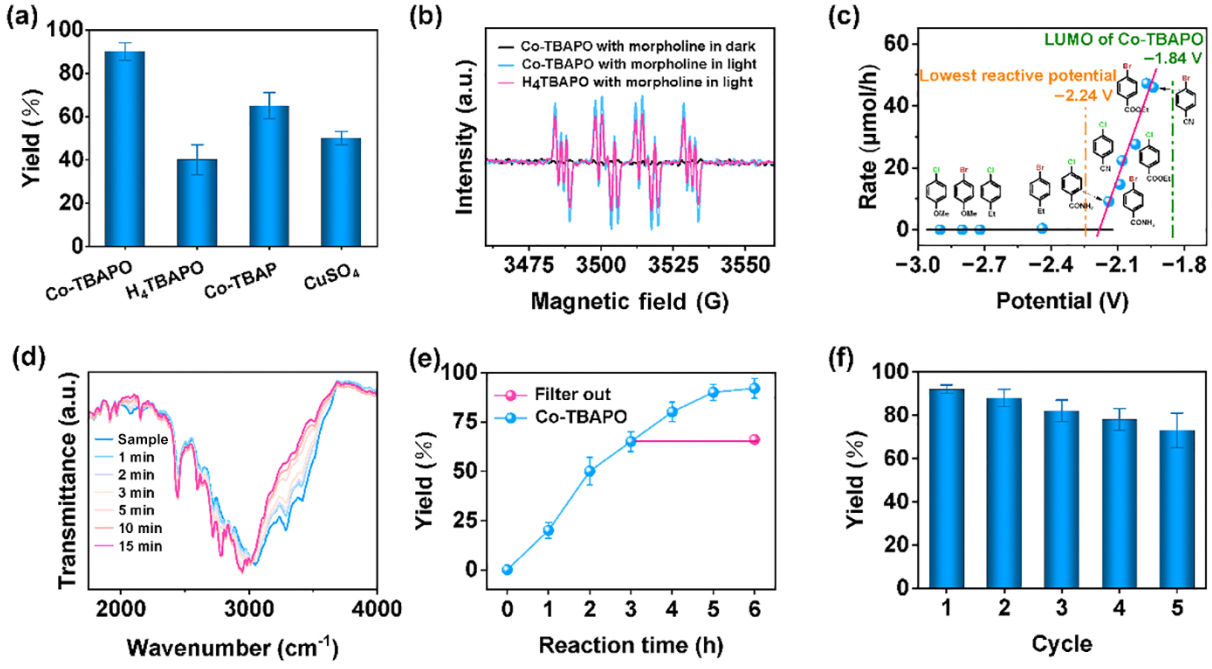

Figure 4 (a) Control experiments of photocatalytic dehalogenation of **1**. (b) The ESR plots of H_4TBAPO and Co-TBAPO with morpholine before and after 395 nm illumination. (c) The corresponding reaction rates of different potential substrates under standard conditions. (d) *In-situ* FT-IR spectra of the system containing Co-TBAPO, substrate **1**, morpholine, and HCOOH under 395 nm irradiation with different times. (e) Yield of photocatalytic reduction of **1** with different conditions. (f) The recycling experiments of Co-TBAPO under the standard conditions.

that Co-TBAPO exhibits higher photocatalytic activity than Co-TBAP (Fig. 3(g)). Replacing Co-TBAPO with Co-TBAP in the experiment under the same conditions, the yield of **1a** decreased to 64% (Fig. 4(a)).

The control experiments showed that photogenerated radicals are vital for this reaction. Electron spin resonance (ESR) measurements revealed that Co-TBAPO exhibits a prominent signal at g = 2.003, even without light (Fig. S22 in the ESM), indicating the presence of an oxygen or nitrogen radical due to the conjugated structure of 2,5-dimethoxybenzene-1,4-diamine in the ligand [60]. This signal was further enhanced under 395 nm illumination, indicating that Co-TBAPO exhibits good photosensitivity and can improve the efficiency of photocatalytic reactions. Upon the introduction of morpholine to the H_4TBAPO ligand, morpholine radicals were detected under illumination after 5 min, indicating that PET process occurred between the ligand and the electron donor morpholine, resulting in morpholine and ligand radicals [61]. Under the same light and time conditions, Co-TBAPO with morpholine exhibited a stronger signal than that of the ligand (Fig. 4(b) and Fig. S23 in the ESM). We infer that the $Co_7(\mu_3\text{-}O)_3$ clusters of Co-TBAPO more effectively promote electron accumulation on the Co-MOFs, improving their photocatalytic activity. $CuSO_4$ effectively quenches photogenerated electrons [62]. Upon the introduction of $CuSO_4$ into the catalytic system under the same conditions, the yield of **1a** decreased to 51% (Fig. 4(a)), indicating that photogenerated electrons are vital for this reaction.

Based on the experimental results and previous studies, we identified a potential mechanistic pathway for photocatalytic dehalogenation reactions with two main steps: dissociation of the C–X bond to generate phenyl radicals and the reduction of the phenyl radicals by active metal hydrogen [55, 63]. To further determine the rate-determining step of the photocatalytic reaction, we measured the substrates with different reduction potentials [12, 13, 64–66]. The results show that brominated and chlorinated reactants that produce the same phenyl radicals have different reaction rates (Fig. 4(c)) and that the reaction rates of substrates with different potentials are directly proportional to their potentials (excluding the reactants, whose potential is much lower than the LUMO of Co-TBAPO), indicating that the reaction rate is determined by the fracture of the C–X bond in the first step. Considering the effect of DMAc on the potential, $E(\mathrm{ArX/(Ar^{\bullet} + X^{-})})$ is approximately 0.4 V higher than $E(\mathrm{ArX/ArX^{\bullet-}})$ in the actual process; thus, the lowest reactive potential of Co-TBAPO is −2.24 V (vs. SCE) (Fig. 4(c)) [65]. Therefore, Co-TBAPO cannot achieve the photocatalytic dehalogenation reduction of substrates with a potential much lower than the LUMO of Co-TBAPO (such as fluorobenzene and aryl halides with electron-rich substituents).

To confirm the proposed mechanism, *in situ* FT-IR spectroscopy was performed to monitor the photocatalytic reaction process (Fig. 4(d) and Fig. S21 in the ESM). Under 395 nm irradiation, the intensity of the characteristic peak at ~ 3400 cm^{-1} (O–H stretching vibration) significantly decreased, indicating that the coordinated water molecules of the Co_7 cluster were effectively removed. The intensity of the characteristic C–Cl stretching vibration at ~ 740 cm^{-1} gradually decreased over time [67], indicating the occurrence of light-triggered reductive cleavage of the C–Cl bonds. Concurrent with the decay of the C–Cl band, a new band appeared in the ~ 2900 cm^{-1} region, characteristic of ν(Co–Cl) stretching vibration, which captures the atomic chlorine transfer from the organic substrate to the cobalt center, forming a Co–Cl intermediate [68]. The new bands that emerged in the 2430–2780 cm^{-1} region can be assigned to Co–NH coordination vibrations that became IR-active due to the generation of unsaturated Co sites upon dehydration [69]. These results indicate that morpholine (or its formate counterpart) initially coordinated to the Co site, activating the

catalyst and facilitating electron donation to form the product. Based on the experimental results, we propose the photocatalytic mechanism shown in Fig. 5. Upon irradiation, the cobalt cluster becomes active via MLCT, reduced by the excited ligands. This facilitates C–Cl bond cleavage and subsequent C–H bond formation, resulting in product formation. Concurrently, the oxidized ligand is regenerated due to electron transfer from the sacrificial electron donor, completing the photocatalytic dehalogenation reduction cycle.

The time-dependent tracing curve shows that the reaction yield increased rapidly to a maximum value within 5 h (Fig. 4(e)). However, the removal of Co-TBAPO after 3 h halted the reaction, and the yield remained constant for another 3 h, indicating that Co-TBAPO is a stable heterogeneous catalyst. Inductively coupled plasma mass spectrometry before and after the reaction revealed a cobalt leaching ratio of 0.21% (Fig. S25 in the ESM), indicating that Co-TBAPO remained stable during the catalytic process and could be used for subsequent experiments. The residual Co-TBAPO from the reaction, recovered by filtration, was used for successive runs. The dehalogenation reduction yield remained approximately 75% after five-cycle experiments, indicating that Co-TBAPO is a good heterogeneous catalyst (Fig. 4(f)). This efficient photocatalytic dehalogenation reduction system was extended to various aryl bromide and aryl chloride compounds (Table 2), and also suitable for halogenated aromatic pollutants (PAHs) [70].

4 Conclusion

In this study, we synthesized, Co-TBAPO, a Co-based MOF for light-driven dehalogenation of aryl halides, achieving a 98% yield of ethyl benzoate in 5 h. The high catalytic efficiency of the MOF can be attributed to the synergistic interaction between the $Co_7(\mu_3\text{-}O)_3$ cluster and the photoactive ligands. *In situ* spectroscopy and kinetic analyses revealed that amine rapidly quenches photogenerated holes, generating radicals. The cluster accepts electrons, breaks the C–X bond, and completes the hydrogenation. The dissociation of the C–X bond determines the reaction rate. Therefore, photocatalytic dehalogenation reduction is suitable for aryl bromide and aryl chloride compounds containing electron-withdrawing groups. This study provides a versatile photocatalytic platform with dual potential for environmental remediation, particularly for the degradation of persistent halogenated organic pollutants under mild, solar-driven conditions, and for sustainable synthetic chemistry.

Electronic Supplementary Material: Supplementary material (synthesis, PXRD, TG, FT-IR, UV–vis, ESR spectra, and ^{1}H NMR) is available in the online version of this article at https://doi.org/10.26599/POM.2026.9140120.

CCDC 2494127 contain the supplementary crystallographic data for this paper. These data can be obtained free of charge via www.ccdc.cam.ac.uk/data_request/cif, by emailing data_request@ccdc.cam.ac.uk.

Data availability

All data needed to support the conclusions in the paper are presented in the manuscript and the Electronic Supplementary Material. Additional data related to this paper may be requested from the corresponding author upon request.

Acknowledgements

This work was financially supported by the National Natural Science Foundation of China (No. 22401073), the Natural Science Foundation of Hebei Province, China (No. B2024205040), Science Research Project of Hebei Education Department (No. BJ2026027), and the foundation of Hebei Normal University (No. L2024B13).

Declaration of competing interest

The authors have no competing interests to declare that are relevant

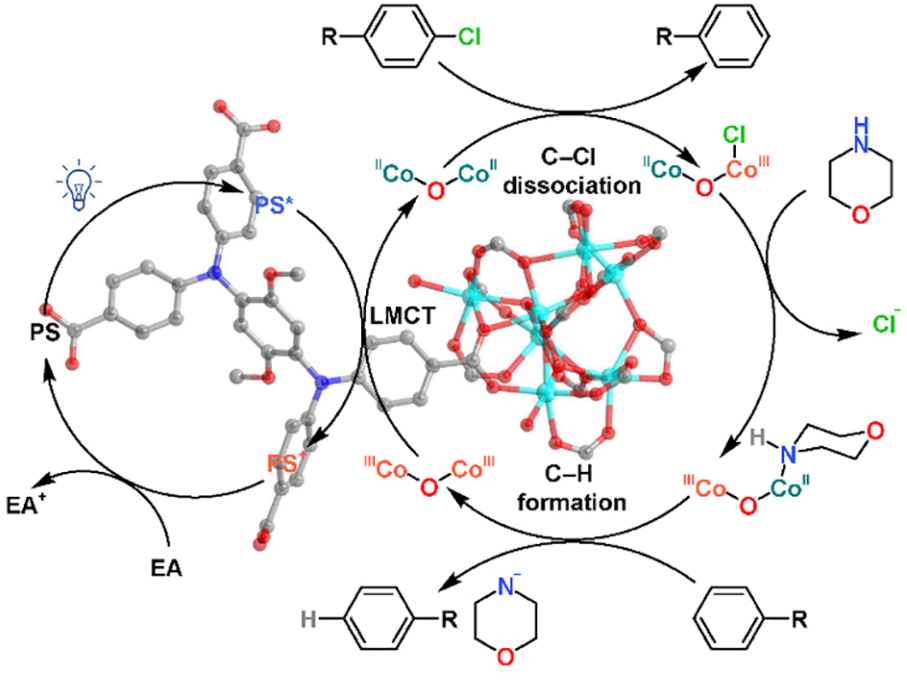

Figure 5 The proposed mechanism for the photocatalytic dehalogenation reaction of halogenated aromatic hydrocarbons under irradiation.

to the content of this article.

Author contribution statement

J. W. W., S. M. L., S. Y. L., Y. Y. W. and L. J. W. designed, performed, and analyzed the experiments. S. M. L., P. C. J., H. T. Y., and J. W. W. co-wrote the manuscript. All the authors have approved the final manuscript.

Use of AI statement

During the preparation of this work, the authors used Deepseek in order to improve the fluency of the article. After using this tool, the authors reviewed and edited the content as needed and takes full responsibility for the content of the publication.

References

[1] Lin, R. H.; Amrute, A. P.; Pérez-Ramírez, J. Halogen-mediated conversion of hydrocarbons to commodities. *Chem. Rev.* **2017**, *117*, 4182–4247.

[2] Liu, H.; Ji, D. W.; Mei, Y. K.; Liu, Y.; Liu, C. H.; Wang, X. Y.; Chen, Q. A. Repurposing of halogenated organic pollutants via alkyl bromide-catalysed transfer chlorination. *Nat. Chem.* **2024**, *16*, 1505–1514.

[3] Wang, Y. Y.; Wei, Y.; Song, W. J.; Chen, C. C.; Zhao, J. C. Photocatalytic hydrodehalogenation for the removal of halogenated aromatic contaminants. *ChemCatChem* **2019**, *11*, 258–268.

[4] Bryden, M. A.; Crovini, E.; Comerford, T.; Studer, A.; Zysman-Colman, E. Organic donor-acceptor thermally activated delayed fluorescence photocatalysts in the photoinduced dehalogenation of aryl halides. *Angew. Chem., Int. Ed.* **2024**, *63*, e202405081.

[5] Agarwal, V.; Miles, Z. D.; Winter, J. M.; Eustáquio, A. S.; El Gamal, A. A.; Moore, B. S. Enzymatic halogenation and dehalogenation reactions: Pervasive and mechanistically diverse. *Chem. Rev.* **2017**, *117*, 5619–5674.

[6] Kubota, K.; Jiang, J. L.; Kamakura, Y.; Hisazumi, R.; Endo, T.; Miura, D.; Kubo, S.; Maeda, S.; Ito, H. Using mechanochemistry to activate commodity plastics as initiators for radical chain reactions of small organic molecules. *J. Am. Chem. Soc.* **2023**, *146*, 1062–1070.

[7] Zhang, Y. T.; Cao, Q. H.; Xi, Y.; Wu, X. Q.; Qu, J. P.; Chen, Y. F. Nickel-catalyzed carbonylative Negishi cross-coupling of unactivated secondary alkyl electrophiles with 1 atm CO gas. *J. Am. Chem. Soc.* **2024**, *146*, 7971–7978.

[8] Islam, N. F.; Borah, D.; Saikia, R.; Gogoi, B.; Sarma, H. Microbial dehalogenation of halogenated organic pollutants: A review. *Environ. Chem. Lett.* **2026**, *24*, 101–137.

[9] Min, H.; Kwon, Y.; Shin, S.; Choi, M.; Mehra, M. K.; Jeon, W.; Kwon, M. S.; Lee, C. W. Tailoring the degradation of cyanoarene-based photocatalysts for enhanced visible-light-driven halogen atom transfer. *Angew. Chem., Int. Ed.* **2024**, *63*, e202406880.

[10] Luo, T.; Jeppesen, H. S.; Schoekel, A.; Bönisch, N.; Xu, F.; Zhuang, R.; Huang, Q.; Senkovska, I.; Bon, V.; Heine, T. et al. Photocatalytic dehalogenation of aryl halides mediated by the flexible metal-organic framework MIL-53(Cr). *Angew. Chem. Int. Ed.* **2025**, *64*, e202422776.

[11] Ma, H.; Han, C. K.; Liu, J. X.; Xu, Y. L.; Chen, C. L.; Zhong, X. H.; Chen, L. Y.; Zhou, R.; Wang, B. Z.; Wang, J. H. et al. Semiconductor cluster with high reduction potential and efficient charge transfer enables visible-light-driven activation of inert organic substrates. *Angew. Chem., Int. Ed.* **2025**, *64*, e202509764.

[12] MacKenzie, I. A.; Wang, L. F.; Onuska, N. P. R.; Williams, O. F.; Begam, K.; Moran, A. M.; Dunietz, B. D.; Nicewicz, D. A. Discovery and characterization of an acridine radical photoreductant. *Nature* **2020**, *580*, 76–80.

[13] Kwon, Y.; Lee, J.; Noh, Y.; Kim, D.; Lee, Y.; Yu, C.; Roldao, J. C.; Feng, S. Y.; Gierschner, J.; Wannemacher, R. et al. Formation and degradation of strongly reducing cyanoarene-based radical anions towards efficient radical anion-mediated photoredox catalysis. *Nat. Commun.* **2023**, *14*, 92.

[14] Natali, M.; Campagna, S.; Scandola, F. Photoinduced electron transfer across molecular bridges: Electron- and hole-transfer superexchange pathways. *Chem. Soc. Rev.* **2014**, *43*, 4005–4018.

[15] Grover, K.; Koblova, A.; Pezacki, A. T.; Chang, C. J.; New, E. J. Small-molecule fluorescent probes for binding- and activity-based sensing of redox-active biological metals. *Chem. Rev.* **2024**, *124*, 5846–5929.

[16] Tian, X. H.; Liu, Y. L.; Yakubov, S.; Schütte, J.; Chiba, S.; Barham, J. P. Photo- and electro-chemical strategies for the activations of strong chemical bonds. *Chem. Soc. Rev.* **2024**, *53*, 263–316.

[17] Wang, J.; Liao, W. R.; Tan, Y.; Henrotte, O.; Kang, Y. C.; Liu, K.; Fu, J. W.; Lin, Z.; Chai, L. Y.; Cortes, E. et al. Transfer dynamics of photo-generated carriers in catalysis. *Chem. Soc. Rev.* **2025**, *54*, 6553–6596.

[18] Atkare, S.; Jagtap, S.; Late, D. J. Exploring the potential of metal-organic framework based composites as key players in bisphenol detection. *Chem. Soc. Rev.* **2025**, *54*, 3736–3774.

[19] Chen, C.; Shen, L. G.; Wang, B. Y.; Lu, X. C.; Raza, S.; Xu, J. J.; Li, B. S.; Lin, H. J.; Chen, B. Environmental applications of metal-organic framework-based three-dimensional macrostructures: A review. *Chem. Soc. Rev.* **2025**, *54*, 2208–2245.

[20] Afshariazar, F.; Morsali, A. Mixed-valence metal-organic frameworks: Concepts, opportunities, and prospects. *Chem. Soc. Rev.* **2025**, *54*, 1318–1383.

[21] Hao, T.; Xu, B.; Wang, X. C.; Zheng, H. R.; Li, S. D.; Wang, F.; Zhang, J. Circularly polarized luminescence enhancement in rare-earth MOFs due to framework chirality and host-guest energy transfer. *Polyoxometalates* **2025**, *4*, 9140095.

[22] White, N. G.; McGuirk, C. M. Defining, designing and determining the structure of supramolecular frameworks. *Chem. Soc. Rev.* **2025**, *54*, 9612–9629.

[23] Sun, N. N.; Shah, S. S. A.; Lin, Z. Y.; Zheng, Y. Z.; Jiao, L.; Jiang, H. L. MOF-based electrocatalysts: An overview from the perspective of structural design. *Chem. Rev.* **2025**, *125*, 2703–2792.

[24] Zhang, D. S.; Wang, L.; Zhang, X. D.; Li, X. B.; Xu, H. X.; Tung, C. H.; Wu, L. Z. Emerging inorganic-organic hybrid photocatalysts for solar-driven overall water splitting: Progress and perspectives. *Chem. Soc. Rev.* **2025**, *54*, 9978–10005.

[25] Navalón, S.; Dhakshinamoorthy, A.; Álvaro, M.; Ferrer, B.; García, H. Metal-organic frameworks as photocatalysts for solar-driven overall water splitting. *Chem. Rev.* **2022**, *123*, 445–490.

[26] Han, G. Y.; Sun, M. S.; Zhao, R. X.; Junaid, Q. M.; Hou, G. Z.; Mohmand, N. Z. K.; Jia, C. M.; Liu, Y. W.; Van Der Voort, P.; Shi, L. et al. Defect engineered Ti-MOFs and their applications. *Chem. Soc. Rev.* **2025**, *54*, 5081–5107.

[27] Troyano, J.; Zamora, F.; Delgado, S. Copper(I)-iodide cluster structures as functional and processable platform materials. *Chem. Soc. Rev.* **2021**, *50*, 4606–4628.

[28] Xu, C. Y.; Pan, Y. T.; Wan, G.; Liu, H.; Wang, L.; Zhou, H.; Yu, S. H.; Jiang, H. L. Turning on visible-light photocatalytic C–H oxidation over metal-organic frameworks by introducing metal-to-cluster charge transfer. *J. Am. Chem. Soc.* **2019**, *141*, 19110–19117.

[29] Zeng, L.; Guo, X. Y.; He, C.; Duan, C. Y. Metal-organic frameworks: Versatile materials for heterogeneous photocatalysis. *ACS Catal.* **2016**, *6*, 7935–7947.

[30] Tang, Y.; Ji, G. F.; Li, H. N.; Gao, H.; He, C.; Zhao, L.; Duan, C. Y. Ligand-regulated photoinduced electron transfer within metal-organic frameworks for efficient photocatalysis. *Inorg. Chem. Front.* **2023**, *10*, 5439–5451.

[31] Song, H.; Guo, M. S.; Wang, J. F.; Liu, Y. Q.; Bi, H. X.; Du, J.; An, W. T.; Ma, Y. Y.; Han, Z. G. Reduced phosphomolybdate as

photoassisted electrochemical crystalline sensor for trace Cr(VI) detection. *Polyoxometalates* **2024**, *3*, 9140065.
[32] Hu, Q. L.; Li, K.; Chen, X. J.; Liu, Y. F.; Yang, G. P. Polyoxometalate catalysts for the synthesis of N-heterocycles. *Polyoxometalates* **2024**, *3*, 9140048.
[33] Wang, F.; Jing, C. J.; Ping, J. J.; He, D. Y.; Shang, W. H.; Zeng, M. L.; Wang, N.; Jia, Z. Y. Polyoxometalate-based Cu(II) complexes as the photocatalyst for oxidation of toluene and photodegradation of metronidazole. *Polyoxometalates* **2024**, *3*, 9140067.
[34] Lei, J.; Yu, Z. L.; Ru, S.; Wang, Z. X.; Li, S.; Luo, N. H.; Huang, J. Z.; Peng, X. P.; Jiang, F.; Wei, Y. G. Decavanadate-catalyzed oxidative cross-dehydrogenative coupling: An efficient and sustainable approach toward P(O)–S bond formation. *Angew. Chem., Int. Ed.* **2025**, *64*, e202507245.
[35] Guo, G. C.; Zhao, J. P.; Guo, S.; Shi, W. X.; Liu, F. C.; Lu, T. B.; Zhang, Z. M. Building Co_{16}-N_3-based UiO-MOF to expand design parameters for MOF photosensitization. *Angew. Chem., Int. Ed.* **2024**, *63*, e202402374.
[36] Yang, G. P.; Liu, Y. F.; Wei, Y. G. Application of polyoxometalates in biomass conversion. *Coord. Chem. Rev.* **2024**, *521*, 216172.
[37] Ni, L. B.; Gu, J.; Jiang, X. Y.; Xu, H. J.; Wu, Z.; Wu, Y. C.; Liu, Y.; Xie, J.; Wei, Y. G.; Diao, G. W. Polyoxometalate-cyclodextrin-based cluster-organic supramolecular framework for polysulfide conversion and guest-host recognition in lithium-sulfur batteries. *Angew. Chem., Int. Ed.* **2023**, *62*, e202306528.
[38] Du, D. Y.; Qin, J. S.; Li, S. L.; Su, Z. M.; Lan, Y. Q. Recent advances in porous polyoxometalate-based metal-organic framework materials. *Chem. Soc. Rev.* **2014**, *43*, 4615–4632.
[39] Yan, X. M.; Xu, J. B.; Zhang, T.; Si, C.; Jiao, J. C.; Li, J.; Han, Q. X. Designing polyoxometalate-based metal-organic framework for oxidation of styrene and cycloaddition of CO_2 with epoxides. *Chin. Chem. Lett.* **2023**, *34*, 107851.
[40] Sun, Z. X.; Wang, R.; Kozhevnikov, I. V. Versatile POMOF-based materials: Synthesis, mechanism, topology and catalytic applications. *Coord. Chem. Rev.* **2025**, *524*, 216304.
[41] Yang, X.; Cui, D. H.; Zhang, T. T.; Liu, Y.; Li, F. Y. LSPR-enhanced photocatalytic N_2 fixation over Z-scheme POMOF-derived Cu/WO_2 modified C–BiOBr with multiple active sites. *Inorg. Chem. Front.* **2024**, *11*, 8246–8257.
[42] Jiao, J. C.; Zhang, L.; Hu, H. N.; Sun, H.; Xu, Z. Q.; Pu, Y. F.; Han, Q. X. Designing a polyoxometalate-pillared metal-organic framework with long-range delocalization for photocatalytic oxidative cross-coupling. *J. Catal.* **2025**, *45*, 116309.
[43] Liu, X. L.; Si, C.; Xu, J. J.; Sun, H.; Li, J.; Han, Q. X. Constructing a polyoxometalate-based metal-organic framework for photocatalytic oxidation of thioethers to sulfoxides utilizing *in situ*-generated superoxide radicals. *Inorg. Chem.* **2025**, *64*, 1263–1271.
[44] Yang, X.; Li, M. H.; Xu, L.; Li, F. Y. Limitation of WO_3 in Zn–Co_3O_4 nanopolyhedra by the pyrolysis of $H_3PW_{12}O_{40}$@BMZIF: Synergistic effect of heterostructure and oxygen vacancies for enhanced nitrogen fixation. *Inorg. Chem.* **2023**, *62*, 8710–8718.
[45] Pimviriyakul, P.; Wongnate, T.; Tinikul, R.; Chaiyen, P. Microbial degradation of halogenated aromatics: Molecular mechanisms and enzymatic reactions. *Microb. Biotechnol.* **2020**, *13*, 67–86.
[46] Ang, T. F.; Maiangwa, J.; Salleh, A. B.; Normi, Y. M.; Leow, T. C. Dehalogenases: From improved performance to potential microbial dehalogenation applications. *Molecules* **2018**, *23*, 1100.
[47] Gao, Z. Y.; Yu, F.; Zhang, M. Y.; Huang, X. Q.; Fu, S. Q.; Azam, M.; Shen, G. D.; Yao, Q. X.; Zhang, Q. D.; Chen, Y. F. et al. Molecular junction polyoxotungstate-based copper-organic frameworks for photocatalytic cross-dehydrogenative coupling. *Angew. Chem., Int. Ed.* **2025**, *64*, e202516079.
[48] Jin, H. G.; Zhao, P. C.; Qian, Y.; Xiao, J. D.; Chao, Z. S.; Jiang, H. L. Metal–organic frameworks for organic transformations by photocatalysis and photothermal catalysis. *Chem. Soc. Rev.* **2024**, *53*, 9378–9418.
[49] Yu, L.; Li, S. F.; Zhou, X.; Zhang, B. C.; Zhou, K.; Xia, Q. B.; Wang, S. J.; Li, J.; Wang, H. Building ultramicroporous zirconium metal-organic frameworks with ligands of high coordination density through a reticular approach. *Nat. Chem.* **2025**, *17*, 1207–1215.
[50] Spek, A. L. Single-crystal structure validation with the program PLATON. *J. Appl. Cryst.* **2003**, *36*, 7–13.
[51] Si, X. Z.; Yao, Q. X.; Pan, X. Z.; Zhang, X. Y.; Zhang, C. L.; Li, Z. Q.; Duan, W. Z.; Hou, J. L.; Huang, X. Q. Mesoporous MOF based on a hexagonal bipyramid Co_8-cluster: High catalytic efficiency on the cycloaddition reaction of CO_2 with bulky epoxides. *Inorg. Chem.* **2023**, *62*, 15006–15014.
[52] Zhao, M. T.; Yuan, K.; Wang, Y.; Li, G. D.; Guo, J.; Gu, L.; Hu, W. P.; Zhao, H. J.; Tang, Z. Y. Metal-organic frameworks as selectivity regulators for hydrogenation reactions. *Nature* **2016**, *539*, 76–80.
[53] Wang, X. K.; Liu, J.; Zhang, L.; Dong, L. Z.; Li, S. L.; Kan, Y. H.; Li, D. S.; Lan, Y. Q. Monometallic catalytic models hosted in stable metal-organic frameworks for tunable CO_2 photoreduction. *ACS Catal.* **2019**, *9*, 1726–1732.
[54] Xia, Q. C.; Yang, J. L.; Zhang, S. Z.; Zhang, J.; Li, Z. Y.; Wang, J. J.; Chen, X. N. Bodipy-based metal-organic frameworks transformed in solid states from 1D chains to 2D layer structures as efficient visible light heterogeneous photocatalysts for forging C–B and C–C bonds. *J. Am. Chem. Soc.* **2023**, *145*, 6123–6134.
[55] Kim, H.; Kim, H.; Lambert, T. H.; Lin, S. Reductive electrophotocatalysis: Merging electricity and light to achieve extreme reduction potentials. *J. Am. Chem. Soc.* **2020**, *142*, 2087–2092.
[56] Tang, Y.; Zhao, L.; Ji, G. F.; Zhang, Y.; He, C.; Wang, Y. F.; Wei, J. W.; Duan, C. Y. Ligand-regulated metal-organic frameworks for synergistic photoredox and nickel catalysis. *Inorg. Chem. Front.* **2022**, *9*, 3116–3129.
[57] Shi, Y. S.; Zhang, T. X.; Jiang, X. M.; Xu, G.; He, C.; Duan, C. Y. Synergistic photoredox and copper catalysis by diode-like coordination polymer with twisted and polar copper-dye conjugation. *Nat. Commun.* **2020**, *11*, 5384.
[58] Ming, M. T.; Wang, Y. C.; Tao, W. X.; Shi, W. J.; Zhong, D. C.; Lu, T. B. Designing dual-atom cobalt catalysts anchored on amino-functionalized MOFs for efficient CO_2 photoreduction. *Green Chem.* **2023**, *25*, 6207–6211.
[59] Zhao, G. Y.; Guo, Y. F.; Huang, P.; Zhang, Z. Z.; Zhao, C. W. Enhanced low-temperature CO oxidation over CuO–Co_3O_4 catalysts promoted with transition metal oxides. *Fuel* **2026**, *403*, 136113.
[60] Yang, B. W.; Chen, Y.; Shi, J. L. Reactive oxygen species (ROS)-based nanomedicine. *Chem. Rev.* **2019**, *119*, 4881–4985.
[61] Dolengovski, E. L.; Gryaznova, T. V.; Sinyashin, O. G.; Gavrilova, E. L.; Kholin, K. V.; Budnikova, Y. H. Morpholine radical in the electrochemical reaction with quinoline N-oxide. *Catalysts* **2023**, *13*, 1279.
[62] De Carvalho, J. G. M.; Geißer, K.; Weishäupl, S. J.; Fischer, R. A.; Pöthig, A. Alkaline earth metal-organic frameworks based on tetratopic anthraquinone-based linkers: Synthesis, characterization, and photochemical applications. *Inorg. Chem.* **2022**, *61*, 15831–15840.
[63] Li, H. C.; Wang, J.; Zhu, W. T.; Li, D. Y.; Li, X. Z.; He, C. Host-guest approach to enhancing photocatalysis via photoinduced energy and electron transfer from a photoactive triphenylamine-based metal-organic cage to bound guests. *Inorg. Chem.* **2025**, *64*, 6621–6630.
[64] Enemærke, R. J.; Christensen, T. B.; Jensen, H.; Daasbjerg, K. Application of a new kinetic method in the investigation of cleavage reactions of haloaromatic radical anions. *J. Chem. Soc., Perkin Trans. 2* **2001**, 1620–1630.
[65] Costentin, C.; Robert, M.; Savéant, J. M. Fragmentation of aryl halide π anion radicals. Bending of the cleaving bond and activation vs driving force relationships. *J. Am. Chem. Soc.* **2004**, *126*, 16051–16057.
[66] Isse, A. A.; Mussini, P. R.; Gennaro, A. New insights into electrocatalysis and dissociative electron transfer mechanisms: The

case of aromatic bromides. *J. Phys. Chem. C* **2009**, *113*, 14983–14992.
[67] McNulty, J.; Nair, J. J.; Cheekoori, S.; Larichev, V.; Capretta, A.; Robertson, A. J. Scope and mechanistic insights into the use of tetradecyl(trihexyl)phosphonium bistriflimide: A remarkably selective ionic liquid solvent for substitution reactions. *Chem.—Eur. J.* **2006**, *12*, 9314–9322.
[68] Morris, M. L.; Busch, D. H. The properties and infrared absorption spectra of complexes of cobalt(III) with pentadentate ethylenediaminetetraacetic acid and hydroxyethylethylenediaminetriacetic acid. *J. Am. Chem. Soc.* **1956**, *78*, 5178–5181.
[69] Beattie, I. R.; Tyrrell, H. J. V. 557. The spectra of some solid cobaltic nitroammines and certain other cobaltic complexes in the 2-15 μ region. *J. Chem. Soc.* **1956**, *56*, 2849–2853.
[70] Zhao, C. X.; Li, A.; Zhang, G. X.; Pan, Y. Y.; Meng, L. L.; Yang, R. Q.; Li, Y. M.; Zhang, Q. H.; Jiang, G. B. Parent and halogenated polycyclic aromatic hydrocarbons in the serum of coal-fired power plant workers: Levels, sex differences, accumulation trends, and risks. *Environ. Sci. Technol.* **2022**, *56*, 12431–12439.

Sumeng Liu is a Master's student at the School of the Hebei Normal University. Her research interests focus on the application of metal-organic frameworks in photocatalysis.

Pengcheng Jiang graduated from Beijing Normal University in 2019 with a Doctor of Science degree. In July 2022, he was introduced to the School of Chemistry and Materials Science at Hebei Normal University as an "elite talent". The research direction is the synthesis of organic functional materials and their applications in the field of organic semiconductors.

Haitao Yu obtained a doctoral degree in Organic Chemistry from the School of Chemistry, Nankai University. He returned to China and started working at the School of Chemistry and Materials Science, Hebei Normal University. Systematic research has been carried out in the fields of organic asymmetric synthesis, organic photochemistry, and the design, synthesis and application research of organic small molecule gels.

Jianwei Wei graduated from Dalian University of Technology, and obtained a doctoral degree. He has since been working at Hebei Normal University (2023–). His research focuses on the application of metal-organic frameworks and metal-organic cages in photoredox catalysis and energy utilization